ACS Energy LETTERS

http://pubs.acs.org/journal/aelccp

Realizing a Mildly Acidic Proton Battery via Surface Functionalization

Jianyong Zhang, Kai Fu, Kai Du, Cheng Wen, Jingyuan Yu, Chunhua Han, Yuxiang Hu, and Lin Xu*

Cite This: *ACS Energy Lett.* 2024, 9, 1853−1862

Read Online

ACCESS | Metrics & More | Article Recommendations | Supporting Information

ABSTRACT: **Aqueous proton batteries (H-ion batteries) hold the potential to fill the gap between batteries and capacitors but suffer from severe electrode material corrosion caused by caustic acid electrolytes. Here, we report a mildly acidic proton battery in which an interfacial functionalization technique together with an ultradiluted H_2SO_4 electrolyte (0.01 M) achieves stable cycle performance of MoO_3 anode materials. The surface functionalization, specifically hydroxyl and carboxyl groups grafted on the interface of MoO_3 electrodes, facilitates successive adsorption and insertion of H^+ and/or H_3O^+ even in proton-deficient electrolytes. The usage of mildly acidic electrolytes obviates the corrosion challenge, achieving promising stable cycle performance of MoO_3 that otherwise rapidly loses capacity in strong acids. The MoO_3//0.01 M H_2SO_4//CuFe-TBA mildly acidic full battery delivers 109.1 mAh g^{-1} capacity after long cycling with 91.18% capacity retention. This work opens an avenue for the rational design of low-corrosion and long-life aqueous proton batteries.**

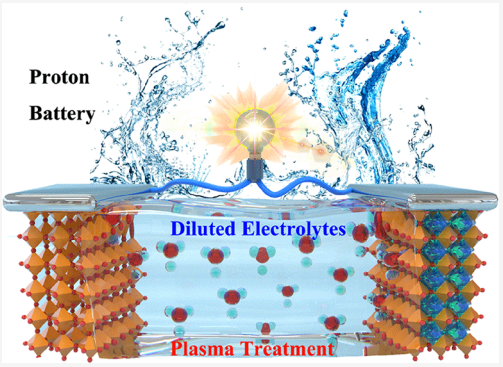

Aqueous proton batteries (APBs) occupy a distinct space in the energy storage territory, in particular, for low-temperature energy storage[1−11] and ultrahigh rate supplies.[12−27] Motivated by the minimal ionic size of H^+ and fascinating Grotthuss conduction topochemistry,[28−37] there has been increasing research interest in proton-insertion electrode materials.[17,18,20−23,25,38−43] In this emerging field, more focus is allocated to research on high-capacity electrode materials.[35,44−47] However, it was soon discovered that the toughest challenge of APB development is that the caustic acid electrolytes corrode most potential electrode materials.[48−59] Moreover, the incompatibility of strong acid solution and commercial battery encapsulation materials hinders the practical application of APBs.[57,60]

Currently, the typical range of acid concentration applied is from 0.1 to 2 M[51−56,61,62] (Table S2, Table S3), essentially due to the rigid demand to ensure a suitable H^+ charge carrier concentration of the electrolyte. These caustic electrolytes inevitably cause piecemeal loss of the active mass of electrodes and associated capacity fading. For example, orthorhombic MoO_3, the state-of-art anode material of APBs, loses 33% of its initial capacity after 100 cycles in solution.[54] Sporadic efforts have been carried out to mitigate the corrosion of electrolytes of APBs, including the usage of weaker phosphoric acid or the exploitation of nonaqueous acetonitrile solvents.[63] However, the cycling stability of MoO_3 in these electrolytes is still unsatisfactory. MoO_3 anode loses 25% of its initial capacity after only 85 cycles in nonaqueous 1.0 M H_3PO_4/acetonitrile electrolyte.[63]

A fundamental question is whether a low-corrosive ultradiluted acidic aqueous solution can serve as an electrolyte for APBs. The answer seems to be no from the perspective of ensuring the concentration of charge carriers in electrolytes. However, the insertion of H^+ and/or H_3O^+ occurs at the interface between the electrode and the electrolyte. If the charge carrier concentration around the interface is consistently maintained at a high level, APBs with ultradiluted acid electrolytes may operate stably. Based on the above speculation, employing surface functionalization that is capable of strongly adsorbing H^+ and/or H_3O^+ at the electrode surface is a promising strategy to realize long-life APBs in low-corrosive ultradiluted acidic electrolytes.

Herein, we report a mildly acidic proton battery that operated stably in a low-corrosive ultradiluted H_2SO_4 solution electrolyte (0.01 M). The surface functionalization, consisting of hydroxyl and carboxyl hydrophilic groups, was constructed through plasma surface modification of the MoO_3 electrode.

Received: November 28, 2023
Revised: March 21, 2024
Accepted: March 27, 2024
Published: April 1, 2024

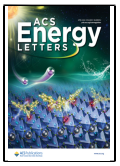

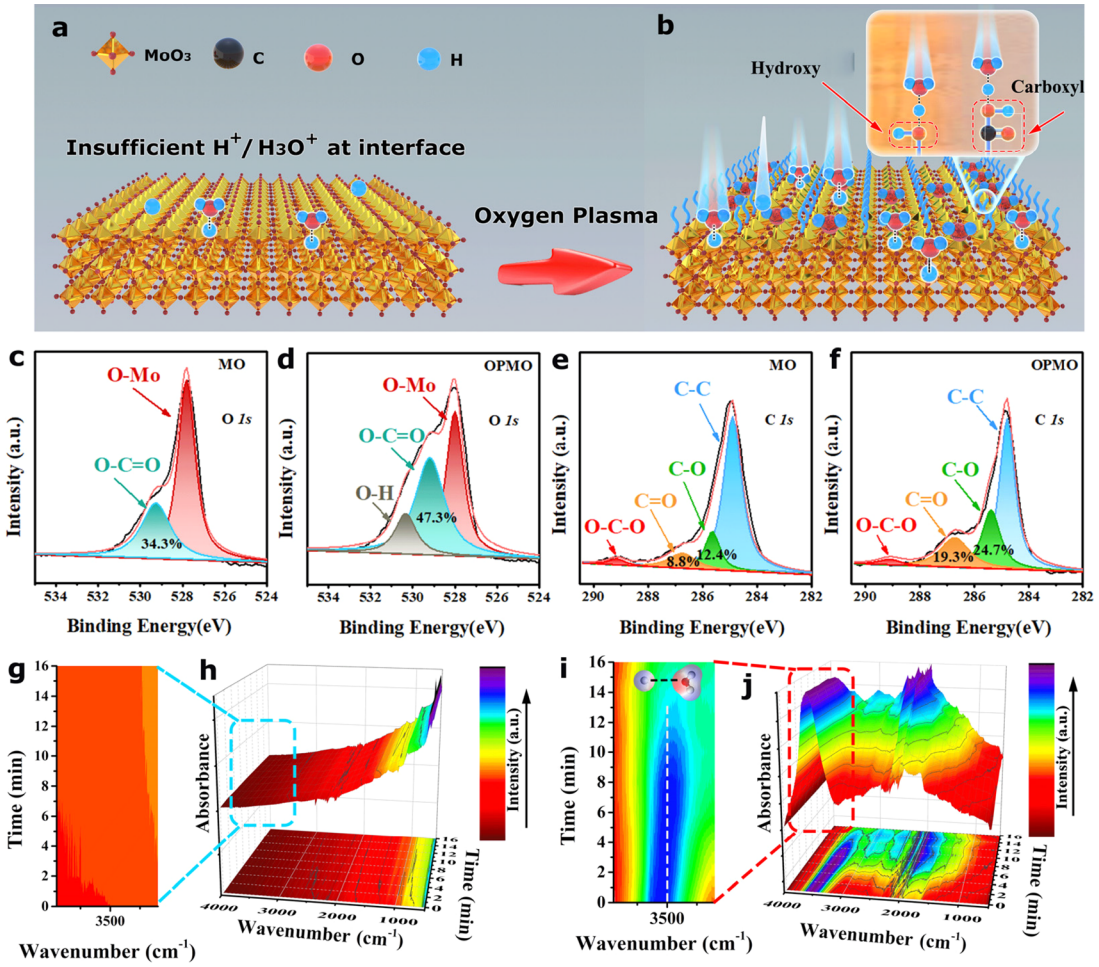

Figure 1. Modification of surface functionalization for MoO_3 electrodes. (a) MoO_3 electrode film. (b) Oxygen plasma treated MoO_3 electrode film. (c, d) O 1s pattern for MO and OPMO. (e, f) C 1s pattern for MO and OPMO. (g, h) In-situ FTIR (infrared spectroscopy) pattern for MO after dipping in 0.01 M H_2SO_4. (i, j) In-situ FTIR pattern for OPMO after dipping in 0.01 M H_2SO_4.

As H^+ and H_3O^+ can be adsorbed on the interface of the electrodes via hydrogen bonds, a localized H^+ rich environment will be created on the interface between the MoO_3 anode and the electrolyte. A successive H^+ and H_3O^+ adsorption−insertion process of MoO_3 was observed in an ultradiluted 0.01 M H_2SO_4 solution. The constructed mildly acidic APB not only tolerates stable operations in ultradiluted acid but also exhibits substantially better reversibility than its strong acidic counterpart. The MoO_3//0.01 M H_2SO_4//CuFe-TBA (TBA = Turnbull's blue analogue) mildly acidic full battery retains a capacity of 109.1 mAh g^{-1} after long cycles with 91.18% retention at 1 A g^{-1}. The feasibility of ultradiluted acid electrolytes and a fundamental understanding of the role of interfacial functional groups provide an avenue for the development of long-life mildly acidic proton batteries.

We aimed to design a surface functionalization to attract charge carriers (protons/hydronium ions) in ultradiluted electrolytes and to enable APB electrodes to work in mildly acidic electrolytes. The oxygen-plasma-treated electrode (OPMO) was prepared after oxygen plasma treatment (plasma cleaner PT-2S, Figure S1) in a Swagelok cell (Figure S2). An illustration of the electrode interface is presented in Figure 1a,b. Due to insufficient charge carriers at the electrode interface in the ultradiluted electrolyte, the MoO_3 electrode (MO) is hardly able to work in the ultradiluted electrolyte (Figure 1a). After the oxygen plasma treatment, the interface of the OPMO forms a series of functional groups such as hydroxyl and carboxyl (Figure 1b). These functional groups attract the charge carriers (hydronium ions and protons) via hydrogen bonds, and they can adsorb protons/hydronium ions from the ultradiluted electrolyte to the electrode interface. As a result, the surface functionalization drives protons and hydrogens to the interface of the electrode successively and enables the MoO_3 electrode to work with sufficient charge carriers in mildly acidic electrolytes. Such a strategy effectively creates a stable working condition for MO electrodes in mildly acidic electrolytes.

To reveal the types of surface functional groups that are created by oxygen plasma, an XPS test was applied to identify them. The O 1s spectra of MO showed 34.3% O═C−O bonds around 529.3 eV (Figure 1c), whereas the O 1s spectra of OPMO exhibited not only 47.3% O═C−O bonds around 529.3 eV[54,56] but also additional O−H bonds at 530.5 eV[57] (Figure 1d). This result demonstrates that hydroxyl and carboxyl groups generated by oxygen plasma treatment lead to an increase in the number of O═C−O and O−H bonds. In addition, the C 1s bonds around 285.5 eV (C−O bonds) and 286.8 eV (C═O bonds) are 12.4% and 8.8% in the MO electrode (Figure 1e),[51] while they increase to 24.7% and 19.3% in OPMO electrode (Figure 1f). This result shows that

https://doi.org/10.1021/acsenergylett.3c02571
ACS Energy Lett. 2024, 9, 1853−1862

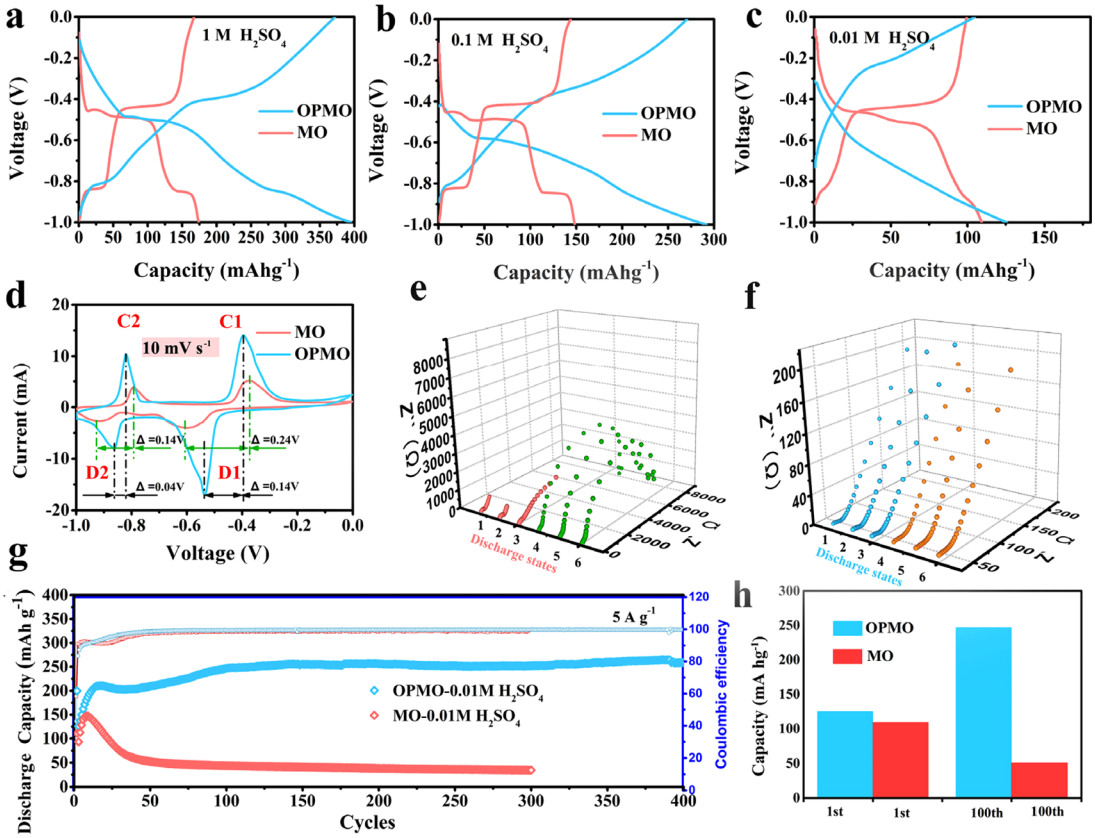

Figure 2. Electrochemical performance of OPMO and MO. (a–c) Galvanostatic charge/discharge (GCD) measurements in 1, 0.1, and 0.01 M H_2SO_4 electrolyte at 5 A g^{-1}. (d) Cyclic voltammetry tests of OPMO and MO (CV) with a mercurous sulfate electrode (MSE) at 10 mV s^{-1}. (e, f) In-situ electrochemical impedance (EIS) plots of the MO electrode and OPMO electrode in the discharge process. (g) Cycling performance of the MO electrode and OPMO electrode in 0.01 M H_2SO_4 at 5 A g^{-1}. (h) Capacity performance in the first cycle and 100th cycle in 0.01 M H_2SO_4. The C rate of the MoO_3 electrode is provided as 1 C = 200 mA g^{-1}.[53]

additional C–O bonds and C═O bonds are attributed to hydroxyl and carboxyl that are produced by oxygen plasma. Besides, an obvious increase in oxygen can be seen in EDS mapping results (Figure S3f–i). As a result, these functional groups, which are grafted on the interface of the electrode, are functional groups that pertain to hydroxyl and carboxyl groups.

To find more evidence to support the in-situ XPS results, the zeta potential of the OPMO was determined. The original hydrophobic electrode interface showed a positive zeta potential with a value of 3.6. Following plasma treatment, the interfacial sulfate became hydrophilic, and the zeta potential of OPMO had a value of −61.5, suggesting that plasma treatment successfully modified the electrode interface. The surface functional groups participate in hydrogen bonds.

To elaborate on the force that motivates interfacial functional groups in the adsorption process, in-situ FTIR was used to examine the acting force of interface groups in ultradiluted electrolytes. The OPMO and MO electrodes were immersed into a mildly acidic electrolyte (0.01 M H_2SO_4) and exposed to air from 0 to 16 min to observe the interfacial characteristics between the electrode and the mildly acidic electrolyte. Typically, the signal of water is located around 3500 cm^{-1} in FTIR spectra, and will occur with symmetric vibration and asymmetric vibration. The asymmetric vibration of water is caused by the formation of hydrogen bonds, and it will lead the FTIR spectrum to shift to a lower wavenumber. In this case, the MO electrode exhibits a hydrophobic interface (Figure S4a) which is unable to adsorb sufficient charge carriers or electrolytes at the interface of the electrode, especially in ultradiluted electrolytes. Hence, there is no obvious signal around 3500 cm^{-1} in the in-situ FTIR spectrum (Figure 1g,h). In contrast, the in-situ FTIR spectrum of the OPMO electrode showed a clear signal around 3500 cm^{-1} (Figure 1i,j) due to its hydrophilic interface (Figure S4b). More importantly, this signal shifts from 3590 to 3420 cm^{-1} in 0–16 min (Figure 1i), demonstrating that the vibration of water is changed from symmetric vibration (3590 cm^{-1}) to asymmetric vibration (3420 cm^{-1}). This asymmetric vibration is caused by the formation of hydrogen bonds between interfacial functional groups and hydronium ions/protons. Consequently, it is believed that the force that drives interfacial functional groups to attract charge carriers in the adsorption process is from hydrogen bonds.

Further, according to the ex-situ measurements, the water contact angle of the electrode changed from a high angle to a low angle during treating time from 0 to 14 min (Figure S3a). The interface properties of the electrode were modified via oxygen plasma. The full Raman spectrum of the OPMO electrode (Figures S3c) demonstrated clear spectrum-fading of the MoO_3 Raman spectra (Figure S3b) and showed no variation in the D and G bands (Figure S3d) when the applied time of oxygen plasma treatment increased. This is attributed to the fact that these functional groups are mainly located at the interface of MoO_3 leading to a decrease in its spectra. Therefore, the dynamic property of the electrode interface is

https://doi.org/10.1021/acsenergylett.3c02571
ACS Energy Lett. 2024, 9, 1853–1862

improved via interfacial functional groups that are grafted on MoO_3.

The morphology of the MoO_3 electrode material is nanowires as shown in SEM and TEM images (Figures S5 and S6), and the Rietveld refinement of MoO_3 (Figure S7) nanowires shows that the phase is α-MoO_3. Moreover, the Ti current collector, which is a more stable current collector than carbon cloth, graphite, glassy carbon, and Pt (Figure S8) in a traditional three-electrode testing cell (Figure S9), delivers a −1.5 to 2.5 V working window. The pH and ionic conductivity of various electrolytes are enumerated as detailed information about electrolytes (Figure S10, Table S1). In ultradiluted electrolytes, the hydronium ions and protons move like cradle balance balls (Figure S11c,d) via Grotthuss conduction, which is identical to traditional high-concentration proton conduction via the well-known Grotthuss conduction (Figure S11a,b). The OPMO remains quite stable in mildly acidic electrolytes (Figure 2g), which certifies that our strategy is effective in making MoO_3 work in mildly acidic electrolytes.[52]

To investigate the electrochemical performance of OPMO and MO, various electrochemical tests were applied to elucidate the function of interfacial functional groups in the insertion process. For a stable electrochemical state comparison, the second cycle is selected. The plots of the first cycle corresponding with Figure 2a,b,c are provided in Figure S12. In the second cycle, GCD plots of OPMO reveal capacities of 395.2, 291.9, and 126 mA h g^{-1} with the rate of 5 A g^{-1} in three different electrolytes (Figure 2a,b,c). This capacity performance is higher than that of the MO electrode (174.1, 148.4, and 109.4 mA h g^{-1}). The observed augmentation in electrode capacity can potentially be attributed to inadequate electrode activation during high current circumstances. This behavior is not present in situations characterized by low electrical current. The electrochemical performance of OPMO was found to be satisfactory at a low current of 0.5 A g^{-1} (Figure S13). The OPMO electrodes exhibited a decrease in electrochemical polarization (Δ0.24 → Δ0.14, Δ0.14 → Δ0.04), which can be attributed to the enhanced dynamic features at the electrode interface by the presence of functional groups. The presence of these functional groups facilitates the movement of protons at the electrode interface, resulting in enhanced dynamic behavior and reduced polarization during the cyclic voltammetry (CV) test.

Notably, the hydrogen evolution reaction (HER) is found in both OPMO and MO electrodes, which might be attributed to the large current causing the HER at the electrode surface. The plasma treatment may be responsible for the obvious HER at OPMO with low Coulombic efficiency in the original 50 cycles in Figure 2g, which is attributed to plasma-induced active sites. And the HER becomes less obvious after 50 cycles with high Coulombic efficiency, attributed to the fact that these active sites are not stable and become disabled after 50 cycles. The active site, like the oxygen vacancy, is the main reason that causes the HER reaction. These active sites are unstable and become less active, which is shown by the gradually increased Coulombic efficiency in Figure 2g. The electrochemical performance gradually stabilized even when the sites became less active, indicating that the electrochemical performance benefits from the carbonyl and hydroxyl groups instead of the active sites.

To compare the electrochemical information on OPMO and MO, the peaks of CV curves were investigated. The comparative analysis of the C-peak and D-peak areas of OPMO electrodes was found to be 49.8% and 50.2%, respectively (Figure 2d), elucidating the high reversible redox reaction of the OPMO electrode. The OPMO redox reaction exhibits sharp and reversible peaks, suggesting that the surface functionalization of the electrode enhances the redox reactions of the electrode. In contrast, the MO sample exhibits rounded reversible redox peaks for the C-peak (49.3%) and D-peak (50.7%), indicating that the redox processes at the interface occur at a sluggish rate. The OPMO electrode exhibits a redox peak that demonstrates a high degree of reversibility. This is evident from the sharp and prominent peaks shown in the cyclic voltammetry (CV) curve, which was obtained at scan rates ranging from 10 to 50 mV s^{-1} (Figure S14). In a word, these results demonstrate that the electrochemical polarization is effectively diminished via surface functionalization, endowing OPMO electrodes with high-capacity performance.

Here, a proportional relationship exists between the peak currents and the square root of the scan rates (Figure S15a), and a nonlinear relationship is observed between the peak currents and the scan rates (Figure S15b), demonstrating that the reaction kinetics of the OPMO electrodes are determined by diffusion control. Generally, when the b value is close to 0.5, it suggests that the electrochemical reaction is diffusion-dominated. When the charge is stored in the electrode, the charge carrier is inserted into the electrode via vehicular transport. When the b value is close to 1.0, it indicates electrode behavior controlled by a surface electrochemical reaction. In this work, the b values of OPMO and MO are close to 0.5 (Figures S16b,f), indicating that the MoO_3 electrode is diffusion-controlled. The b value of OPMO is higher than that of MO (Figure S16c) in 0.01 M H_2SO_4 indicating that the dynamic property of OPMO is higher than that of MO in diluted electrolytes. The OPMO in 2 M H_2SO_4 shows a higher b value than the OPMO in 0.01 M H_2SO_4, which is attributed to the fact that the higher concentration of the electrolyte shows higher dynamic properties.

To demonstrate the interfacial electrochemical properties, OPMO and MO were further studied by in-situ EIS. The radii of semicircles in the in-situ EIS plots correspond to interface resistance.[64−66] The radii of the semicircles in the MO electrode exhibited an escalating trend (∼2000) during discharge processes (Figure 2e), whereas in the OPMO electrode (Figure 2f), the radii of semicircles exhibited very small values in discharge processes, revealing that the OPMO electrode presents a higher ionic diffusion rate than the MO electrode. The angle of the Nyquist plot for OPMO (Figure S17b) is higher than that of MO (Figure S17a), revealing that the dynamic properties, of OPMO are higher than those of MO. To further investigate interfacial dynamic properties, the 2D plots of in-situ EIS were investigated with Warburg impedance (Figures S16d and S17a). The Warburg impedance is part of the diffusion impedance and is a diagonal segment of the diffusion impedance spectrum with a slope of curves. The Warburg factors of OPMO and MO are shown in the in-situ EIS (Figure S17b,c). The slope value of the MO electrode was reduced from 1.46 to 0.22, suggesting that the interface diffusion rate is inadequate and experienced a significant decrease during the electrochemical procedure. On the other hand, the slope of OPMO remained very stable, ranging from 1.67 to 1.65. This observation suggests that the interface diffusion rate of the OPMO is noteworthy and remains consistent during the electrochemical reaction. This phenom-

https://doi.org/10.1021/acsenergylett.3c02571
ACS Energy Lett. 2024, 9, 1853−1862

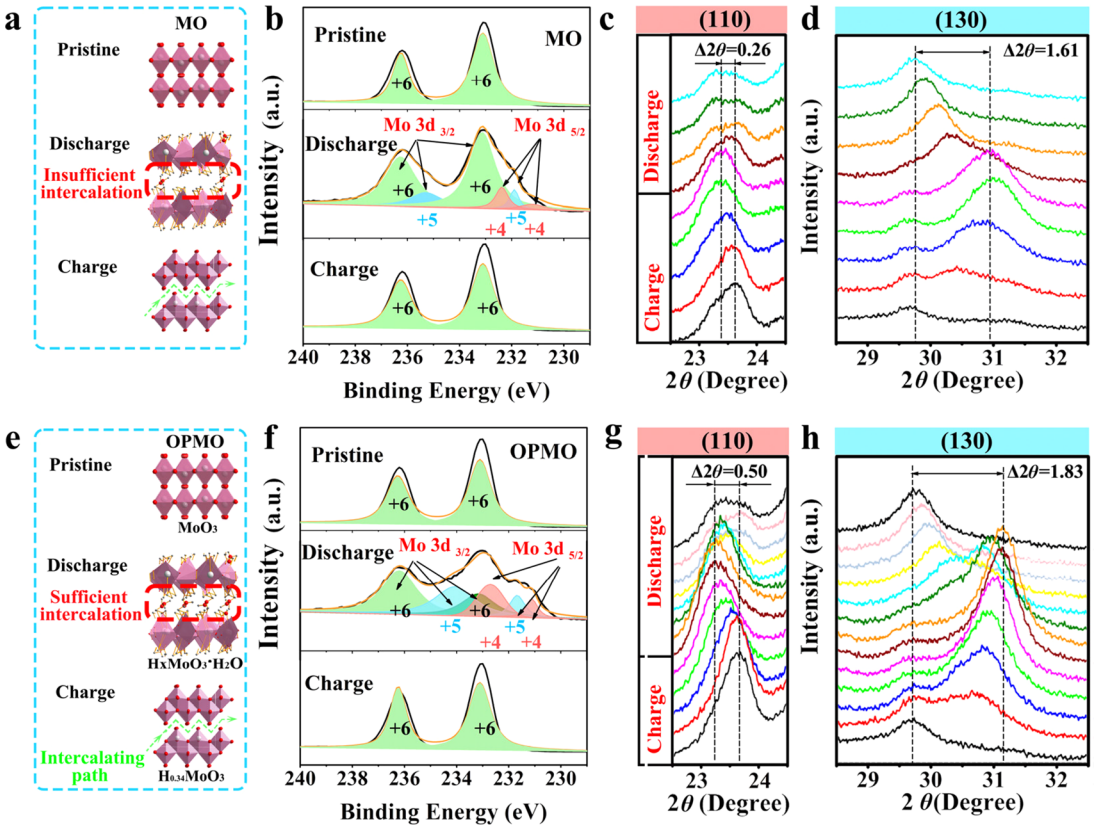

Figure 3. Structure evolution during discharge/charge. (a) Schematic illustration of the MO crystal structure in pristine/discharge/charge states. (b) XPS investigation of the Mo 3d peak in pristine/discharge/charge states. (c, d) In-situ XRD studies of the MO electrode in the (110) peak and (130) peak during charge/discharge. (e) Schematic illustration of the OPMO crystal structure in pristine/discharge/charge states. (f) XPS investigation of the Mo 3d peak for OPMO in pristine/discharge/charge states. (g, h) In-situ XRD studies of the OPMO electrode in the (110) peak and (130) peak during charge/discharge.

enon is derived from the presence of the interfacial functional groups.

Additionally, the electrochemical impedance spectra (EIS) of OPMO and MO were investigated (Figure S18). This investigation serves as additional evidence to support our findings. The EIS test was applied to identify the interfacial diffusion features of MO (Figure S18a) and OPMO (Figure S18c). The results obtained from EIS also indicate that the interface diffusion impedance of OPMO (with a value of k = 4.2, Figure S18d) is higher compared to that of MO (with a value of k = 0.58, Figure S18b).

The cycling plot of the MO electrode drops drastically (Figure 2g). In contrast, the cycling performance of the OPMO electrode delivers 259 mA h g^{-1} after 400 cycles in 0.01 M H_2SO_4, signifying that the electrochemical performance of OPMO is more stable than that of MO. OPMO electrode showed satisfactory stability in 0.01 M H_2SO_4 electrolyte compared with the MO electrode in Figure 2g. The electrochemical performance of the high-mass lading electrodes demonstrated around 250 mAh g^{-1} after 300 cycles (Figure S19b), which is close to the electrochemical result of low-mass loading (Figure S19a). The electrochemical performance of plasma-treated electrodes is not influenced when the mass loading increases. The samples were further tested in 1 M $(NH_4)_2SO_4$. The MO delivered a capacity of 28, 14, and 9 mAh g^{-1} for 1, 17, and 35 cycles (Figure S20b). The OPMO delivered a capacity of 77, 31, and 13 mAh g^{-1} for 1, 17, 35 cycles (Figure S20c). The OPMO showed higher capacity than the MO, indicating that the plasma enhanced the capacity performance of the MoO_3 electrode in 1 M $(NH_4)_2SO_4$. Both electrodes showed poor electrochemical performance because α-MoO_3 shows poor cycling performance in the storage of NH_4^+ ions.

The escalating capacity performance might be attributed to activation of the electrode at a high rate. The comparison of capacity performance is enumerated as a bar graph (Figure 2h), which clearly illustrates that interfacial functional groups provide an obvious enhancement for MoO_3 electrochemical performance. The MO electrode shows dramatic dissolution in strong acid Figure S21, while the interfacial functional groups effectively inhibited the dissolution issue in mildly acidic electrolytes. As a result, interfacial functional groups, which are grafted on the interface of electrodes, improved the electrochemical performance efficaciously in mildly acidic electrolytes.

To enhance comprehension of the electrochemical performance of plasma modification of the electrode, a TBA electrode was subjected to oxygen plasma treatment. The capacity performance of the oxygen-plasma treated TBA electrode (OP-TBA) was improved from 101 to 118.5 mAh g^{-1} (Figure S22). The increase in capacity performance can be attributed to the application of plasma treatment.[67] In addition, plasma-treated TBA was tested in the 0.01 M H_2SO_4 electrolyte. The voltage–capacity curves remain unchanged from the first to the 100th cycle (Figure S23) and demonstrated 97% capacity retention for 100 cycles (Figure S24). These results suggested that plasma-treated TBA showed stable electrochemical perform-

https://doi.org/10.1021/acsenergylett.3c02571
ACS Energy Lett. 2024, 9, 1853−1862

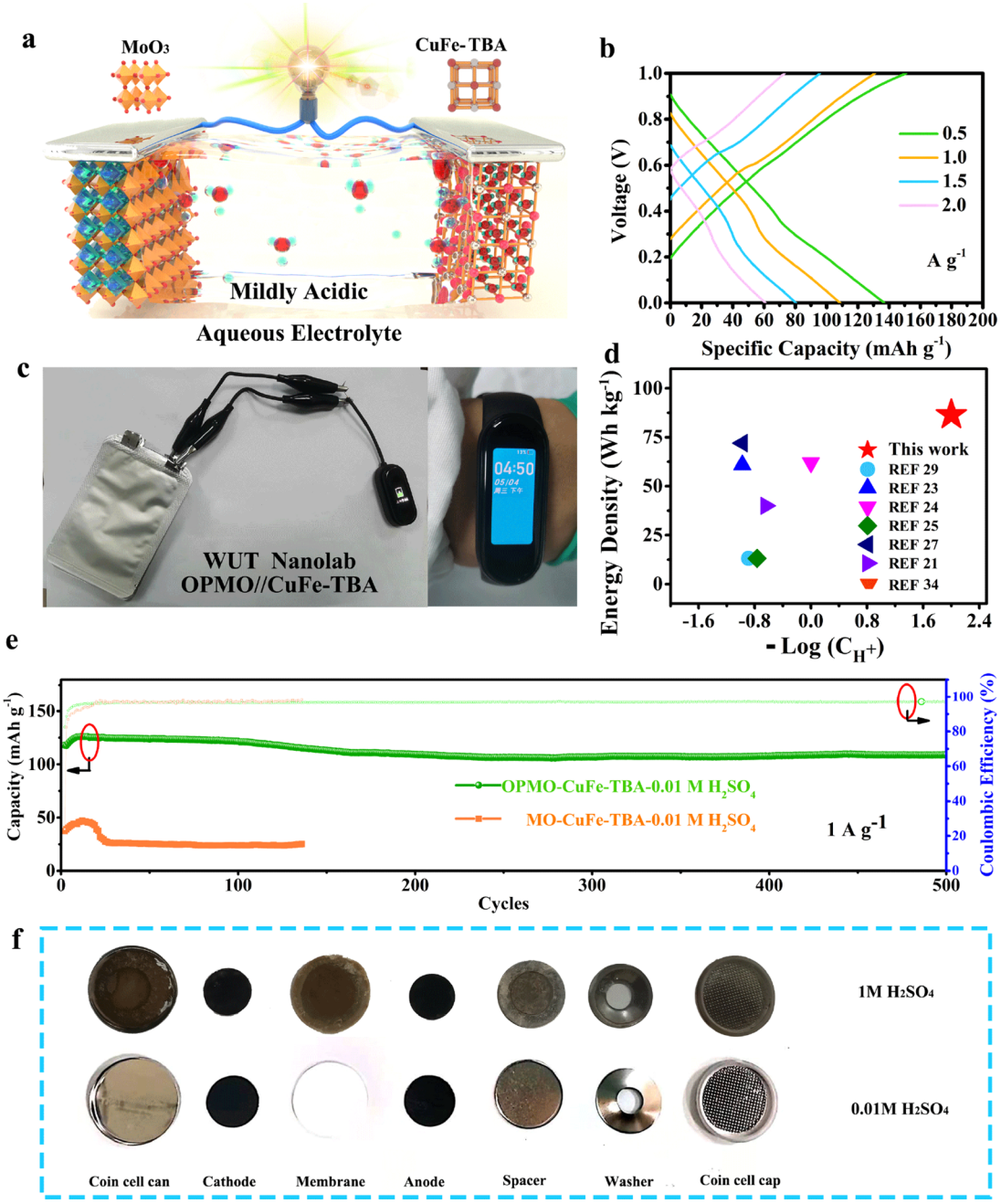

Figure 4. Electrochemical performance and application of the OPMO//CuFe-TBA full battery. (a) Schematic illustration for full APB. (b) GCD curves for full APB. (c) Full battery application in an electronic watch with eight series-connection cells. (d) Electrochemical performance of this work compared to current APBs. (e) Electrochemical performances of OPMO-CuFe-TBA and MO-CuFe-TBA at the rate of 1 A g^{-1}. (f) Corrosivity tests for the coin cell in 0.01 M H_2SO_4 and 1 M H_2SO_4.

ance in a diluted acid solution. Thus, the plasma treatment has the potential to be applied to other kinds of electrodes in proton batteries.

To elaborate the relationships between the electrochemical performance of electrodes and the function of interfacial functional groups, ex-situ XPS and in-situ XRD tests were applied to investigate the valence shifts and crystal structure evolution of electrodes. First, the electrochemical processes, with schematic illustration in Figure 3a,e, are divided into three states (pristine/discharge/charge) that correspond to the crystal structure of the electrode. In the discharge process, the crystal structure of the MO electrode shows insufficient intercalation between layer spaces in Figure 3a (red dotted box). For the OPMO electrode, the crystal structure exhibits sufficient intercalation in the layer spaces during the discharge process (red dotted box in Figure 3e). The reason for this is attributed to interfacial functional groups imposing more charge carriers into the interlayer structure of the OPMO electrode in the discharge process. To demonstrate this, we applied ex-situ XPS to investigate the valence shifts of Mo during charge/discharge. In the discharge process (Figure 3b), XPS spectra of Mo 3d peaks show low peaks relating to Mo^{5+} and Mo^{4+}. In contrast, XPS spectra of OPMO present high and obvious peaks due to Mo^{5+} and Mo^{4+} in the discharge process (Figure 3f), which demonstrates that the OPMO electrode delivers more obvious valence shifts ($Mo^{6+} \rightarrow Mo^{5+} \rightarrow Mo^{4+}$)

https://doi.org/10.1021/acsenergylett.3c02571
ACS Energy Lett. 2024, 9, 1853−1862

than MO during the discharge process. This result is attributed to the fact that intercalation of more charge carriers leads to a more obvious redox reaction. Therefore, the excellent electrochemical performance of OPMO is ascribed to the interfacial functional groups impelling more charge carriers like hydronium ions and protons to intercalate into OPMO electrodes, leading to high-capacity performance.

Importantly, this phenomenon was demonstrated via in-situ XRD patterns as well. According to Bragg's law, the peak of the XRD pattern relates to the lattice plane of the crystal structure and the shifts of it during the charge/discharge process correspond to the variation of layer spacing. The shifts of the (110) peak in OPMO present a wider value (0.50) than those of the MO electrode (0.26) during the discharge−charge process (Figure 3c,g). Simultaneously, it shows a similar variation at the (130) peak (Figure 3d,h). The shifts of the (130) peak in OPMO display larger variations (1.83) than those of MO (1.61). The large shifts in the XRD pattern are caused by the intercalation of more charge carriers, especially for charge carriers with large radii such as hydronium ions. The stark difference in the in-situ XRD can be seen in the capacity difference shown in Figure 4e at the same current density of 1 A g^{-1}. The stark peak variation in Figure 3h is around 1.83° when the capacity difference is 70 mA h g^{-1} in Figure 4e. More importantly, it was found that the OPMO electrode delivered obvious peaks of $H_xMoO_3{\cdot}H_2O$ that were previously undiscovered in the discharge process (Figure S25a,b), revealing that more hydronium ions and protons are inserted into the lattice of the electrode via interfacial functional groups in mildly acidic electrolyte. As a result, ex-situ XPS and in-situ XRD results revealed that interfacial functional groups attract more hydronium ions/protons to intercalate into the OPMO electrode, leading to higher electrochemical performance than the pristine electrode.

To demonstrate that both hydronium ions and protons are inserted into the OPMO electrode, the electrochemical reaction of the electrode was studied via in-situ XRD. A digital photo of the testing cell and device is shown in Figure S26, and a schematic illustration of the charge/discharge processes is presented in Figure S27a,e. The time−voltage curves are shown in Figure S27c,f. To be specific, the XRD pattern of the initial electrode is shown by the cyan line (Figure S27d), and the full discharge stage is shown as a green line (Figure S27d). The dark blue line (Figure S27d) is related to the charging process (Figure S27b). Herein, it was found that the electrode delivered an obvious crystal-water phase as $H_xMoO_3{\cdot}H_2O$ in the discharge process (Figure S27e,g), indicating that both hydronium ions and protons are co-inserted into the lattice of the electrode. According to the XRD patterns during the charge/discharge process, electrochemical reactions of OPMO are believed to be $MoO_3 \rightarrow H_xMoO_3{\cdot}H_2O \rightarrow H_{0.34}MoO_3$ in the first cycle (the x = 1.68).[55] Interestingly, the phase of the OPMO electrode becomes $H_{0.34}MoO_3$ instead of MoO_3 after the first discharge (Figure S27d), suggesting that a few protons (0.34 mol) are inserted irreversibly in MoO_3. Specifically, the original phase of the electrode was MoO_3 before cycling (Figure S27d, curve ①), and the phase of the electrode shifted to $H_{0.34}MoO_3$ after the first cycle (Figure S27d, curve ③). The peak at 25.5° (010) moved to 25.1° irreversibly after the first cycle (Figure S27d), which verified the phase variation of $MoO_3 \rightarrow H_{0.34}MoO_3$. More importantly, the OH that is attributed to crystal water is found in the OPMO electrode after discharging and resting at room temperature for 20 days (Figure S27h). Further, the insertion of hydronium ions is higher than that of protons after the first cycle because a few protons insert into the layer structure of the electrode irreversibly in the first cycle. An intercalation path (Figure 3e) is formed after the first cycle (Figure S28). The electrochemical reactions of the electrode in the charge−discharge process are believed to be as follows:

$$MoO_3 \xrightarrow[\text{First cycle}]{H_3O^+,H^+} H_{0.34}MoO_3 \xleftrightarrow{H_3O^+,H^+} H_xMoO_3{\cdot}H_2O$$

To find more evidence to support the in-situ XRD results, a quartz crystal microbalance (QCM) was applied to investigate the electrode variation during the electrochemical process. The QCM results corresponding to the CV curves are shown in Figure S29a. The first cycle QCM results showed that the mass change started at 0 ng and ended around 40 ng in the mass change curve (Figure S29a), indicating that there was an irreversible mass change (40 ng) in the first cycle. This irreversible mass change corresponded to the in-situ XRD results. In addition, the second cycle started around 40 ng instead of 0 ng (Figure S29b) at 0 V, which also demonstrated that the electrode had an irreversible mass change in the first cycle. QCM tests were performed to monitor the operando mass change and identify the active charge carriers. In aqueous solutions, protons are mostly bonded to water to form hydronium ions, which can influence the surface electrochemistry and induce overall mass changes in electrodes. Because the proton (H^+) itself has negligible weight, the mass change can be mostly attributed to the adsorption of hydronium with electrodes.

To answer the question of mass change with the intercalation/deintercalation of the charge carrier, detailed mass change information is exhibited with the discharge and charge processes in Figure S29b. In the discharging process, the mass of the electrode increased from 40 to 100 ng at the C1 peak (Figure S29b) as an up-arrow. Then, the mass of the electrode increased from 63 ng to 70 ng at the C2 peak (Figure S29b) as an up-arrow. The mass change curves in C1 and C2 demonstrate the fact that the mass of the electrode increased when charges were inserted into the electrode during discharge. In the charging process, the mass of the electrode decreased from 36 ng to 31 ng at the A1 peak (Figure S29b) as a down-arrow. Then, the mass of the electrode decreased from 10 to 2 ng at the A2 peak (Figure S29b) as a down-arrow. The mass change curves in A1 and A2 indicate that the mass of the electrode decreased when charges were deinserted from the electrode during charging. In conclusion, these results are in accordance with the fact that the electrode mass increased when the charge was inserted and reduced when the charge was deinserted.

Notably, the mass change is attributed to hydronium and water, and the charge change is attributed to hydronium. What is interesting is that there is a mass increase but no charge change at A1′, indicating that water is adsorbed into the electrode. This result means that the A1′ peak is the process by which the electrode adsorbs water in the charging process.

To investigate the electrochemical performance of a full APB, a full battery was provided as $OPMO//H_2SO_4//CuFe\text{-}TBA$ with a graphic illustration given in Figure 4a. The CuFe-TBA exhibited a cubic shape around 100 nm (Figure S30), and the XRD pattern corresponds to the pure CuFe-TBA phase[68] with the PDF card of PDF #01-0244 (Figure S31).[16] Besides, the CuFe-TBA half-cell in 0.01 M H_2SO_4 exhibits a discharge

https://doi.org/10.1021/acsenergylett.3c02571
ACS Energy Lett. 2024, 9, 1853−1862

voltage of ~0.6 V (Figure S32). As for the full battery, it delivered 0.75 V voltage (Figure S33) and tested as 0.92 V (Figure S34) after the first charge immediately. The full cell exhibited 137, 107, 80, and 61 mA h g^{-1} at rates of 0.5, 1.0, 1.5, and 2.0 A g^{-1} (Figure 4b) corresponding with Figure S35. The full battery delivered a 109.1 mAh g^{-1} capacity after long cycling at 1 A g^{-1} (Figure 4e). The modified battery maintained 91.18% of its initial capacity. This full battery was capable of being applied to electronic watches (Figure 4c) and could be further applied to the LED and LCD (Figures S36 and S37), suggesting that our research provides a promising energy device that applies to safe, stable, and long life-span. It delivers a high power density (81.27 Wh kg^{-1}) compared with current APBs (Figure 4d).[58] The recently reported APBs are listed in Tables S2 and S3 for better comprehension. The mildly acidic electrolytes show no etching to the battery shell (Figure 4f, Figure S38), delivering a wider application to APB electrodes, battery encapsulations, current collectors, and test devices.[69] The full cell shows less self-discharge phenomenon after resting for 24 h (Figure S39), indicating that the cell is able to be applied as an energy storage device with less self-discharge issue. Overall, the electrochemical properties of APB electrodes were successfully improved. Our research endows a significant enhancement to APB research.

In conclusion, this work elaborately explains the interface chemistry of interfacial functional groups that enable MoO_3 to work stably in mildly acidic electrolytes. It was found that interfacial functional groups, which are assembled in an electrode interface, promoted the adsorption of charge carriers in the ultradiluted electrolyte according to the in-situ FTIR results and led to co-intercalation of protons and hydronium ions based on ex-situ XPS and in-situ XRD results. Realizing the application of mildly acidic electrolytes enhances the life span of APB electrodes and breaks the limitation of current highly corrosive APB electrolytes. Besides, the utility of ultradiluted acidic electrolytes widens the potential application in numerous undiscovered electrodes and extends the application in battery encapsulations, current collectors, and test devices, which will promote rapid development for APB research in the near future. In the end, revealing the interfacial functional group's interface chemistry may lead to an instructive inspiration in the design of long-life-span APBs and may guide the practical construction of APBs.

■ ASSOCIATED CONTENT

Supporting Information

The Supporting Information is available free of charge at https://pubs.acs.org/doi/10.1021/acsenergylett.3c02571.

Experimental section, digital photos of the plasma treatment process and Swagelok cell, additional characterization of the materials (XRD patterns, SEM images, digital photos, XPS spectra, FTIR spectra test), additional electrochemical data (EIS profiles, capacity performance, the rate performance of the full battery), and a digital photo of the OPMO-TBA pouch cell (PDF)

■ AUTHOR INFORMATION

Corresponding Author

Lin Xu − *State Key Laboratory of Advanced Technology for Materials Synthesis and Processing, School of Materials Science and Engineering, Wuhan University of Technology, Wuhan 430070, China; Hubei Longzhong Laboratory, Wuhan University of Technology (Xiangyang Demonstration Zone), Xiangyang 441000 Hubei, China; Hainan Institute, Wuhan University of Technology, Sanya 572000, China;* orcid.org/0000-0003-2347-288X; Email: linxu@whut.edu.cn

Authors

Jianyong Zhang − *State Key Laboratory of Advanced Technology for Materials Synthesis and Processing, School of Materials Science and Engineering, Wuhan University of Technology, Wuhan 430070, China*

Kai Fu − *State Key Laboratory of Advanced Technology for Materials Synthesis and Processing, School of Materials Science and Engineering, Wuhan University of Technology, Wuhan 430070, China*

Kai Du − *Key Laboratory of Advanced Functional Materials of Education Ministry of China, College of Materials Science and Engineering, Beijing University of Technology, Beijing 100124, China*

Cheng Wen − *State Key Laboratory of Advanced Technology for Materials Synthesis and Processing, School of Materials Science and Engineering, Wuhan University of Technology, Wuhan 430070, China*

Jingyuan Yu − *State Key Laboratory of Advanced Technology for Materials Synthesis and Processing, School of Materials Science and Engineering, Wuhan University of Technology, Wuhan 430070, China*

Chunhua Han − *State Key Laboratory of Advanced Technology for Materials Synthesis and Processing, School of Materials Science and Engineering, Wuhan University of Technology, Wuhan 430070, China*

Yuxiang Hu − *Key Laboratory of Advanced Functional Materials of Education Ministry of China, College of Materials Science and Engineering, Beijing University of Technology, Beijing 100124, China;* orcid.org/0000-0001-5641-0357

Complete contact information is available at: https://pubs.acs.org/10.1021/acsenergylett.3c02571

Notes

The authors declare no competing financial interest.

■ ACKNOWLEDGMENTS

This work was supported by the National Natural Science Foundation of China (52272234, 52172233), the National Key Research and Development Program of China (2020YFA0715000), the Key Research and Development Program of Hubei Province (2021BAA070), and the Independent Innovation Project of Hubei Longzhong Laboratory (2022ZZ-20).

■ REFERENCES

(1) Guo, Z. W.; Huang, J. H.; Dong, X. L.; Xia, Y. Y.; Yan, L.; Wang, Z.; Wang, Y. G. An organic/inorganic electrode-based hydronium-ion battery. *Nat. Commun.* **2020**, *11* (1), 959.

(2) Shi, M. M.; Das, P.; Wu, Z. S.; Liu, T. G.; Zhang, X. Y. Aqueous Organic Batteries Using the Proton as a Charge Carrier. *Adv. Mater.* **2023**, *35*, No. 2302199.

(3) Zhou, L.; Liu, L.; Hao, Z.; Yan, Z.; Yu, X.-F.; Chu, P. K.; Zhang, K.; Chen, J. Opportunities and challenges for aqueous metal-proton batteries. *Matter* **2021**, *4* (4), 1252−1273.

(4) Li, J.; Yan, H. H.; Xu, C. W.; Liu, Y. W.; Zhang, X. K.; Xia, M. T.; Zhang, L. Y.; Shu, J. Insights into host materials for aqueous proton batteries: structure, mechanism and prospect. *Nano Energy* **2021**, *89*, No. 106400.
(5) Xu, T.; Wang, D.; Li, Z.; Chen, Z.; Zhang, J.; Hu, T.; Zhang, X.; Shen, L. Electrochemical Proton Storage: From Fundamental Understanding to Materials to Devices. *Nano-Micro Letters* **2022**, *14* (1), 126.
(6) Xu, Y.; Wu, X.; Ji, X. The Renaissance of Proton Batteries. *Small Structures* **2021**, *2*, No. 2000113.
(7) Cai, Z.; Wang, J.; Sun, Y. Anode corrosion in aqueous Zn metal batteries. *eScience* **2023**, *3* (1), No. 100093.
(8) Jin, J.; Yang, L.; Chen, F.; Gu, N. Drug delivery system based on nanobubbles. *Interdisciplinary Materials* **2022**, *1* (4), 471−494.
(9) Sato, T.; Yoshikawa, K.; Zhao, W.; Kobayashi, T.; Rajendra, H. B.; Yonemura, M.; Yabuuchi, N. Efficient Stabilization of Na Storage Reversibility by Ti Integration into O′3-Type $NaMnO_2$. *Energy Material Advances* **2021**, *21*, 9857563.
(10) Cheng, H.; Wang, J.; Wu, C.; Liu, Z. Electrocatalysts for Formic Acid-Powered PEM Fuel Cells: Challenges and Prospects. *Energy Material Advances* **2023**, *4*, No. 0067.
(11) Schmuch, R.; Wagner, R.; Hörpel, G.; Placke, T.; Winter, M. Performance and cost of materials for lithium-based rechargeable automotive batteries. *Nat. Energy* **2018**, *3* (4), 267−278.
(12) Wu, X.; Qiu, S.; Xu, Y.; Ma, L.; Bi, X.; Yuan, Y.; Wu, T.; Shahbazian-Yassar, R.; Lu, J.; Ji, X. Hydrous nickel−iron turnbull's blue as a high-rate and low-temperature proton electrode. *ACS Appl. Mater. Interfaces* **2020**, *12* (8), 9201−9208.
(13) Lukatskaya, M. R.; Kota, S.; Lin, Z. F.; Zhao, M. Q.; Shpigel, N.; Levi, M. D.; Halim, J.; Taberna, P. L.; Barsoum, M.; Simon, P.; Gogotsi, Y. Ultra-high-rate pseudocapacitive energy storage in two-dimensional transition metal carbides. *Nat. Energy* **2017**, *2* (8), No. 17105.
(14) Halverson, A. F.; Zhu, K.; Erslev, P. T.; Kim, J. Y.; Neale, N. R.; Frank, A. J. Perturbation of the electron transport mechanism by proton intercalation in nanoporous TiO_2 films. *Nano Lett.* **2012**, *12* (4), 2112−2116.
(15) Chen, Z.; Peng, Y.; Liu, F.; Le, Z.; Zhu, J.; Shen, G.; Zhang, D.; Wen, M.; Xiao, S.; Liu, C. P.; Lu, Y.; Li, H. Hierarchical nanostructured WO_3 with biomimetic proton channels and mixed ionic-electronic conductivity for electrochemical energy storage. *Nano Lett.* **2015**, *15* (10), 6802−8.
(16) Wu, X.; Hong, J. J.; Shin, W.; Ma, L.; Liu, T.; Bi, X.; Yuan, Y.; Qi, Y.; Surta, T. W.; Huang, W.; Neuefeind, J.; Wu, T.; Greaney, P. A.; Lu, J.; Ji, X. Diffusion-free Grotthuss topochemistry for high-rate and long-life proton batteries. *Nat. Energy* **2019**, *4* (2), 123−130.
(17) Xu, Y.; Zheng, Y.; Wang, C.; Chen, Q. An all-organic aqueous battery powered by adsorbed quinone. *ACS Appl. Mater. Interfaces* **2019**, *11* (26), 23222−23228.
(18) Tong, L.; Jing, Y.; Gordon, R. G.; Aziz, M. J. Symmetric all-quinone aqueous battery. *ACS Appl. Energy Mater.* **2019**, *2* (6), 4016−4021.
(19) Yang, X.; Ni, Y.; Lu, Y.; Zhang, Q.; Hou, J.; Yang, G.; Liu, X.; Xie, W.; Yan, Z.; Zhao, Q.; Chen, J. Designing Quinone-Based Anodes with Rapid Kinetics for Rechargeable Proton Batteries. *Angew. Chem., Int. Ed.* **2022**, *61* (39), No. e202209642.
(20) Yue, F.; Tie, Z.; Deng, S.; Wang, S.; Yang, M.; Niu, Z. An ultralow temperature aqueous battery with proton chemistry. *Angew. Chem., Int. Ed.* **2021**, *60* (25), 13882−13886.
(21) Nueangnoraj, K.; Tomai, T.; Nishihara, H.; Kyotani, T.; Honma, I. An organic proton battery employing two redox-active quinones trapped within the nanochannels of zeolite-templated carbon. *Carbon* **2016**, *107*, 831−836.
(22) Christudas Dargily, N.; Thimmappa, R.; Manzoor Bhat, Z.; Devendrachari, M. C.; Kottaichamy, A. R.; Gautam, M.; Shafi, S. P.; Thotiyl, M. O. A rechargeable hydrogen battery. *J. Phys. Chem. Lett.* **2018**, *9* (10), 2492−2497.
(23) Bitenc, J.; Košir, U.; Vizintin, A.; Lindahl, N.; Krajnc, A.; Pirnat, K.; Jerman, I.; Dominko, R. Electrochemical Mechanism of Al Metal−Organic Battery Based on Phenanthrenequinone. *Energy Material Advances* **2021**, *21*, 9793209.
(24) Yu, J. Z.; Li, J.; Leong, Z. Y.; Li, D. S.; Lu, J.; Wang, Q.; Yang, H. Y. A crystalline dihydroxyanthraquinone anodic material for proton batteries. *Materials Today Energy* **2021**, *22*, No. 100872.
(25) Liang, Y.; Jing, Y.; Gheytani, S.; Lee, K. Y.; Liu, P.; Facchetti, A.; Yao, Y. Universal quinone electrodes for long cycle life aqueous rechargeable batteries. *Nat. Mater.* **2017**, *16* (8), 841−848.
(26) Wan, X.; Song, Y.; Zhou, H.; Shao, M. Layered Double Hydroxides for Oxygen Evolution Reaction towards Efficient Hydrogen Generation. *Energy Material Advances* **2022**, *10*, 9842610.
(27) Sun, T.; Du, H.; Zheng, S.; Shi, J.; Yuan, X.; Li, L.; Tao, Z. Bipolar Organic Polymer for High Performance Symmetric Aqueous Proton Battery. *Small Methods* **2021**, *5* (8), No. e2100367.
(28) Wang, H.; Emanuelsson, R.; Karlsson, C.; Jannasch, P.; Stromme, M.; Sjodin, M. Rocking-chair proton batteries with conducting redox polymer active materials and protic ionic liquid electrolytes. *ACS Appl. Mater. Interfaces* **2021**, *13* (16), 19099−19108.
(29) Zhu, M.; Zhao, L.; Ran, Q.; Zhang, Y.; Peng, R.; Lu, G.; Jia, X.; Chao, D.; Wang, C. Bioinspired Catechol-Grafting PEDOT Cathode for an All-Polymer Aqueous Proton Battery with High Voltage and Outstanding Rate Capacity. *Adv. Sci.* **2022**, *9* (4), No. e2103896.
(30) Strietzel, C.; Sterby, M.; Huang, H.; Stromme, M.; Emanuelsson, R.; Sjodin, M. An aqueous conducting redox-polymer-based proton battery that can withstand rapid constant-voltage charging and sub-zero temperatures. *Angew. Chem., Int. Ed.* **2020**, *59* (24), 9631−9638.
(31) Wang, X.; Zhou, J.; Tang, W. Poly(dithieno[3,2-b:2′,3′-d]pyrrole) twisting redox pendants enabling high current durability in all-organic proton battery. *Energy Storage Mater.* **2021**, *36*, 1−9.
(32) Emanuelsson, R.; Sterby, M.; Stromme, M.; Sjodin, M. An all-organic proton battery. *J. Am. Chem. Soc.* **2017**, *139* (13), 4828−4834.
(33) Navarro-Suárez, A. M.; Carretero-González, J.; Rojo, T.; Armand, M. Poly(quinone-amine)/nanocarbon composite electrodes with enhanced proton storage capacity. *J. Mater. Chem. A* **2017**, *5* (44), 23292−23298.
(34) Sun, T.; Du, H.; Zheng, S.; Shi, J.; Tao, Z. High Power and Energy Density Aqueous Proton Battery Operated at −90 °C. *Adv. Funct. Mater.* **2021**, *31* (16), No. 2010127.
(35) Tie, Z.; Liu, L.; Deng, S.; Zhao, D.; Niu, Z. Proton insertion chemistry of a zinc-organic battery. *Angew. Chem., Int. Ed.* **2020**, *59* (12), 4920−4924.
(36) Wang, X.; Bommier, C.; Jian, Z.; Li, Z.; Chandrabose, R. S.; Rodriguez-Perez, I. A.; Greaney, P. A.; Ji, X. Hydronium-ion batteries with perylenetetracarboxylic dianhydride crystals as an electrode. *Angew. Chem., Int. Ed.* **2017**, *56* (11), 2909−2913.
(37) Qiao, J.; Qin, M.; Shen, Y. M.; Cao, J.; Chen, Z.; Xu, J. A rechargeable aqueous proton battery based on a dipyridophenazine anode and an indium hexacyanoferrate cathode. *Chem. Commun.* **2021**, *57* (35), 4307−4310.
(38) Fleischmann, S.; Sun, Y.; Osti, N. C.; Wang, R.; Mamontov, E.; Jiang, D.-e.; Augustyn, V. Interlayer separation in hydrogen titanates enables electrochemical proton intercalation. *J. Mater. Chem. A* **2020**, *8* (1), 412−421.
(39) Jiang, H.; Hong, J. J.; Wu, X.; Surta, T. W.; Qi, Y.; Dong, S.; Li, Z.; Leonard, D. P.; Holoubek, J. J.; Wong, J. C.; Razink, J. J.; Zhang, X.; Ji, X. Insights on the proton insertion mechanism in the electrode of hexagonal tungsten oxide hydrate. *J. Am. Chem. Soc.* **2018**, *140* (37), 11556−11559.
(40) Kang, S.; Singh, A.; Reeves, K. G.; Badot, J.-C.; Durand-Vidal, S.; Legein, C.; Body, M.; Dubrunfaut, O.; Borkiewicz, O. J.; Tremblay, B.; Laberty-Robert, C.; Dambournet, D. Hydronium ions stabilized in a titanate-layered structure with high ionic conductivity: Application to aqueous proton batteries. *Chem. Mater.* **2020**, *32* (21), 9458−9469.
(41) Wang, S.; Zhao, X.; Yan, X.; Xiao, Z.; Liu, C.; Zhang, Y.; Yang, X. Regulating fast anionic redox for high-voltage aqueous hydrogen-ion-based energy storage. *Angew. Chem., Int. Ed.* **2019**, *58* (1), 205−210.

https://doi.org/10.1021/acsenergylett.3c02571
ACS Energy Lett. 2024, 9, 1853−1862

(42) Sun, T.; Du, H.; Zheng, S.; Shi, J.; Tao, Z. High power and energy density aqueous proton battery operated at − 90 °C. *Adv. Funct. Mater.* **2021**, *31*, No. 2010127.
(43) Lemaire, P.; Sel, O.; Alves Dalla Corte, D.; Iadecola, A.; Perrot, H.; Tarascon, J. M. Elucidating the origin of the electrochemical capacity in a proton-based battery H_xIrO_4 via advanced electrogravimetry. *ACS Appl. Mater. Interfaces* **2020**, *12* (4), 4510−4519.
(44) Yue, F.; Tie, Z.; Zhang, Y.; Bi, S.; Wang, Y.; Niu, Z. Proton Chemistry Induced Long-Cycle Air Self-Charging Aqueous Batteries. *Angew. Chem., Int. Ed.* **2022**, *61* (40), No. e202208513.
(45) Shen, D.; Rao, A. M.; Zhou, J.; Lu, B. High-Potential Cathodes with Nitrogen Active Centres for Quasi-Solid Proton-Ion Batteries. *Angew. Chem., Int. Ed.* **2022**, *134*, No. e202201972.
(46) Shen, D.; Rao, A. M.; Zhou, J.; Lu, B. High-Potential Cathodes with Nitrogen Active Centres for Quasi-Solid Proton-Ion Batteries. *Angew. Chem., Int. Ed.* **2022**, *61* (22), No. e202201972.
(47) Tie, Z.; Deng, S.; Cao, H.; Yao, M.; Niu, Z.; Chen, J. A Symmetric All-Organic Proton Battery in Mild Electrolyte. *Angew. Chem., Int. Ed.* **2022**, *61* (8), No. e202115180.
(48) Yan, L.; Huang, J.; Guo, Z.; Dong, X.; Wang, Z.; Wang, Y. Solid-state proton battery operated at ultralow temperature. *ACS Energy Lett.* **2020**, *5* (2), 685−691.
(49) Liang, G.; Wang, Y.; Huang, Z.; Mo, F.; Li, X.; Yang, Q.; Wang, D.; Li, H.; Chen, S.; Zhi, C. Initiating hexagonal MoO_3 for superb-stable and fast NH_4^+ storage based on hydrogen bond chemistry. *Adv. Mater.* **2020**, *32* (14), No. 1907802.
(50) Fan, H.; Liu, K.; Zhang, X.; Di, Y.; Liu, P.; Li, J.; Hu, B.; Li, H.; Ravivarma, M.; Song, J. Spatial structure regulation towards armor-clad five-membered pyrroline nitroxides catholyte for long-life aqueous organic redox flow batteries. *eScience* **2023**, *1*, 100202.
(51) Jiang, H.; Shin, W.; Ma, L.; Hong, J. J.; Wei, Z.; Liu, Y.; Zhang, S.; Wu, X.; Xu, Y.; Guo, Q.; Subramanian, M. A.; Stickle, W. F.; Wu, T.; Lu, J.; Ji, X. A high-rate aqueous proton battery delivering power below −78 °C via an unfrozen phosphoric acid. *Adv. Energy Mater.* **2020**, *10* (28), No. 2000968.
(52) Wang, C.; Zhao, S.; Song, X.; Wang, N.; Peng, H.; Su, J.; Zeng, S.; Xu, X.; Yang, J. Suppressed Dissolution and Enhanced Desolvation in Core−Shell MoO_3 @TiO_2 Nanorods as a High-Rate and Long-Life Anode Material for Proton Batteries. *Adv. Energy Mater.* **2022**, *12* (19), No. 2200157.
(53) Su, Z.; Ren, W.; Guo, H.; Peng, X.; Chen, X.; Zhao, C. Ultrahigh areal capacity hydrogen-ion batteries with MoO_3 loading over 90 mg cm^{-2}. *Adv. Funct. Mater.* **2020**, *30* (46), No. 2005477.
(54) Wang, X. F.; Xie, Y. M.; Tang, K.; Wang, C.; Yan, C. L. Redox Chemistry of Molybdenum Trioxide for Ultrafast Hydrogen-Ion Storage. *Angew. Chem. Int. Edit* **2018**, *57* (36), 11569−11573.
(55) Guo, H.; Goonetilleke, D.; Sharma, N.; Ren, W.; Su, Z.; Rawal, A.; Zhao, C. Two-Phase Electrochemical Proton Transport and Storage in α-MoO_3 for Proton Batteries. *Cell Reports Physical Science* **2020**, *1* (10), No. 100225.
(56) Ma, N.; Kosasang, S.; Yoshida, A.; Horike, S. Proton-conductive coordination polymer glass for solid-state anhydrous proton batteries. *Chem. Sci.* **2021**, *12*, 5818−5824.
(57) Su, Z.; Chen, J.; Ren, W.; Guo, H.; Jia, C.; Yin, S.; Ho, J.; Zhao, C. "Water-in-sugar" electrolytes enable ultrafast and stable electrochemical naked proton storage. *Small* **2021**, *17* (40), No. e2102375.
(58) Su, Z.; Chen, J.; Stansby, J.; Jia, C.; Zhao, T.; Tang, J.; Fang, Y.; Rawal, A.; Ho, J.; Zhao, C. Hydrogen-Bond Disrupting Electrolytes for Fast and Stable Proton Batteries. *Small* **2022**, *18* (22), No. e2201449.
(59) Wu, S.; Chen, J.; Su, Z.; Guo, H.; Zhao, T.; Jia, C.; Stansby, J.; Tang, J.; Rawal, A.; Fang, Y.; Ho, J.; Zhao, C. Molecular Crowding Electrolytes for Stable Proton Batteries. *Small* **2022**, No. e2202992.
(60) Wang, S.; Jiang, H.; Dong, Y.; Clarkson, D.; Zhu, H.; Settens, C. M.; Ren, Y.; Nguyen, T.; Han, F.; Fan, W.; Kim, S. Y.; Zhang, J.; Xue, W.; Sandstrom, S. K.; Xu, G.; Tekoglu, E.; Li, M.; Deng, S.; Liu, Q.; Greenbaum, S. G.; Ji, X.; Gao, T.; Li, J. Acid-in-clay electrolyte for wide-temperature-range and long-cycle proton batteries. *Adv. Mater.* **2022**, *34*, No. e2202063.
(61) Qiao, Q.; Wang, H.-J.; Li, C.-P.; Wang, X.-Z.; Ren, X.-M. Improving proton conduction of the Prussian blue analogue $Cu_3[Co(CN)_6]_2 \cdot nH_2O$ at low humidity by forming hydrogel composites. *Inorg. Chem. Front.* **2021**, *8* (9), 2305−2314.
(62) Peng, X.; Guo, H.; Ren, W.; Su, Z.; Zhao, C. Vanadium hexacyanoferrate as high-capacity cathode for fast proton storage. *Chem. Commun.* **2020**, *56* (79), 11803−11806.
(63) Xu, Y.; Wu, X.; Jiang, H.; Tang, L.; Koga, K. Y.; Fang, C.; Lu, J.; Ji, X. A non-aqueous H_3Po_4 electrolyte enables stable cycling of proton electrodes. *Angew. Chem., Int. Ed.* **2020**, *59* (49), 22007−22011.
(64) Zhang, J.; Cao, Y.; Ou, X.; Zhang, J.; Wang, C.; Peng, C.; Zhang, B.; Tian, Y. Constituting the NASICON type solid electrolyte coated material forming anti-high voltage system to enhance the high cut-off voltage performance of $LiNi_{0.6}Co_{0.2}Mn_{0.2}O_2$ via charge attracts electrostatic assembly. *J. Power Sources* **2019**, *436*, No. 226722.
(65) Zhang, J.; Zhang, J.; Liu, J.; Cao, Y.; Huang, C.; Ji, G.; Zhao, Z.; Ou, X.; Zhang, B. Environmentally phase-controlled stratagem for open framework pyrophosphate anode materials in battery energy storage. *Journal of Materials Chemistry C* **2021**, *9* (29), 9147−9157.
(66) Zhang, J.; Zhang, J.; Ou, X.; Wang, C.; Peng, C.; Zhang, B. Enhancing high-voltage performance of ni-rich cathode by surface modification of self-assembled nasicon fast ionic conductor $LiZr_2(PO_4)_3$. *ACS Appl. Mater. Interfaces* **2019**, *11* (17), 15507−15516.
(67) Zhang, Y.; Rawat, R. S.; Fan, H. J. Plasma for Rapid Conversion Reactions and Surface Modification of Electrode Materials. *Small Methods* **2017**, *1* (9), No. 1700164.
(68) Kim, H.; Choi, W.; Yoon, J.; Um, J. H.; Lee, W.; Kim, J.; Cabana, J.; Yoon, W. S. Exploring anomalous charge storage in anode materials for next-generation li rechargeable batteries. *Chem. Rev.* **2020**, *120* (14), 6934−6976.
(69) Zhu, Z.; Wang, W.; Yin, Y.; Meng, Y.; Liu, Z.; Jiang, T.; Peng, Q.; Sun, J.; Chen, W. An ultrafast and ultra-low-temperature hydrogen gas-proton battery. *J. Am. Chem. Soc.* **2021**, *143* (48), 20302−20308.

https://doi.org/10.1021/acsenergylett.3c02571
ACS Energy Lett. 2024, 9, 1853−1862